Improving the SST in a regional ocean model through refined SST assimilation

Silje Christine Iversen[1], Ann Kristin Sperrevik[2], and Olivier Goux[3]

[1]Department of Physics and Technology, Arctic University of Norway, Tromsø, Norway
[2]Division for Ocean and Ice, Norwegian Meteorological Institute, Oslo, Norway
[3]CERFACS/CECI CNRS UMR 5318, Toulouse, France

Correspondence: Silje Christine Iversen (silje.c.iversen@uit.no)

Abstract. Infrared (IR) and passive microwave (PMW) satellite sea surface temperature (SST) retrievals are valuable to assimilate into high-resolution regional ocean forecast models. Still, there are issues related to these SSTs that need to be addressed to achieve improved ocean forecasts. Firstly, satellite SST products tend to be biased. Assimilating SSTs from different providers can thus cause the ocean model to receive inconsistent information. Secondly, while the PMW SSTs are valuable for con-

5 straining the model in cloudy regions, the spatial resolution of these retrievals is rather coarse. Assimilating PMW SSTs into high-resolution ocean models will spatially smooth the modeled SST and consequently remove finer SST structures. In this study, we implement a bias correction scheme which corrects the satellite SSTs before assimilation. We also introduce a special observation operator, called the supermod operator, into the Regional Ocean Modeling System (ROMS) 4-dimensional variational data assimilation algorithm. This supermod operator handles the resolution mismatch between the coarse observations and the finer model. We test the bias correction scheme and the supermod operator using a setup of ROMS covering the shelf

10 seas and shelf break off Norway. The results show that the validation statistics in the modeled SST improve if we apply the bias correction scheme. We also find improvements in the validation statistics when we assimilate PMW SSTs in conjunction with the IR SSTs. However, our supermod operator must be activated to avoid smoothing the modeled SST structures of spatial scales smaller than twice the PMW SST footprint. Both the bias correction scheme and the supermod operator are easy to

15 apply, and the supermod operator can be adapted for other observation variables.

1 Introduction

Satellite-based sea surface temperature (SST) retrievals account for the majority of observations assimilated into ocean forecast models and can be retrieved by measuring both the infrared (IR) and passive microwave (PMW) radiation emitted by the ocean

20 surface. In cloudy regions such as high northern latitudes, the cloud coverage reduces the number of SST retrievals by the IR sensors. Consequently, SSTs from PMW radiometers serve as a complementary data set as the PMW radiation penetrates

clouds. While the spatial resolution of IR SSTs typically is similar to or finer than those of regional ocean forecast models, a disadvantage with the PMW SSTs is their relatively coarse resolution.

Indeed, mesoscale ocean models can resolve circulation features of smaller spatial scales than those the PMW SSTs can pro-
vide. Such differences in resolved scales are commonly referred to as representation errors within the field of data assimilation (Janjić et al., 2018). Previous studies have considered the differences in resolved scales while assimilating coarse observations such as those of sea ice concentration, satellite sea surface salinity, and scatterometer ocean surface winds (Buehner et al., 2013; Martin et al., 2019; Mile et al., 2021). Furthermore, the difference between the footprint sizes of the PMW and IR SSTs has been considered while producing global SST analyses where IR and PMW SSTs are merged using statistical methods (Donlon
et al., 2012; Brasnett and Colan, 2016). However, an attempt with regards to assimilating PMW SSTs into a high-resolution regional ocean forecast model has so far not been undertaken.

We implement a special observation operator, called the supermod operator, into the Regional Ocean Modeling System (ROMS; Haidvogel et al., 2008; Shchepetkin and McWilliams, 2009) 4-dimensional variational (4D-Var) data assimilation system (Moore et al., 2011; Gürol et al., 2014). This operator considers the resolution mismatch between the PMW SSTs and
the model by comparing each PMW SST observation with the model mean over an area similar to the observation footprint. We show that, compared to a traditional observation operator, the supermod operator prevents PMW SSTs from constraining the spatial scales of the model that the PMW SSTs do not resolve properly. Thus, the supermod operator enables us to assimilate PMW SSTs without smoothing the modeled SST structures. We test the operator using a configuration of ROMS that covers the shelf seas and shelf break off Norway. This region is subject to high cloud coverage, meaning that there is a need for
assimilating PMW SSTs to constrain the model. Moreover, the risk of smoothing modeled SST structures is high in this region since the spatial scales of the SST structures typically are small at high latitudes.

To further improve the modeled SST, we take into account that satellite SSTs from different providers tend to be biased due to differences and limitations in the SST retrieval processes and algorithms (Chan and Gao, 2005; Høyer et al., 2012; Wang et al., 2016). Specifically, we implement a bias correction scheme which is inspired by Høyer et al. (2014) and use this scheme
to correct the assimilated satellite SST observations for biases. The scheme ensures consistency between SST observations from different providers, thus preventing the model from receiving inconsistent information during the assimilation of different satellite SST products. By reducing the inconsistent information, the probability of artificial noise in the modeled SST is hampered.

2 Data and methods

2.1 Model configuration and data assimilation setup

We use a configuration of ROMS to model the shelf seas and shelf break off Norway (Fig. 1). ROMS is a free-surface, hydrostatic, primitive equation ocean model using stretched, terrain-following vertical coordinates, which is beneficial for modeling shallow, coastal waters. We present only a brief summary of the model configuration since a thorough description can be found in Röhrs et al. (2018).
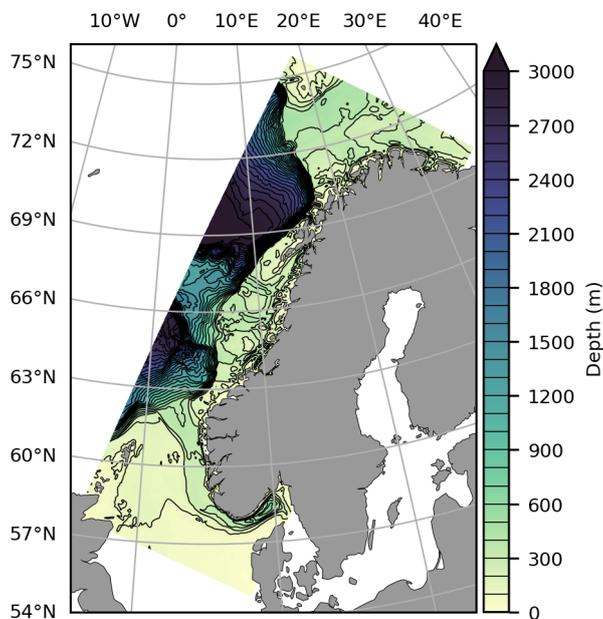
Figure 1. Bathymetry of the model region covering the shelf seas and shelf break off Norway.

55   The horizontal resolution of the model is 2.4 km, and there are 42 layers in the vertical direction which are distributed so that the uppermost layer has a thickness of ~ 0.2–1.2 m. Vertical mixing is parameterized using a second-order scheme for turbulent kinetic energy and a generic length-scale (GLS) based on a setup recommended by Umlauf and Burchard (2005) and Warner et al. (2005). The configuration differs slightly from that of Röhrs et al. (2018) with different choices for the *Kmin* and *Pmin* parameters, which in our case are set to 1.0×10^{-8}.

60   We force the model with three-hourly operational forecast data from the Integrated Forecast System of the European Centre for Medium-Range Weather Forecasts (ECMWF, 2016). Air–sea fluxes for momentum and heat are calculated via the COARE3.0 bulk flux algorithms (Fairall et al., 2003) within ROMS. Open boundary conditions consist of daily averages of all state variables from the TOPAZ4 reanalysis (Xie et al., 2017). The sea surface elevation and currents are adjusted to include the effect of local atmospheric pressure, as TOPAZ4 does not include the inverse barometer effect. Harmonic tidal forcing,

65 consisting of eight tidal constituents from the TPXO9 global inverse barotropic model (Egbert and Erofeeva, 2002), is also imposed along the open boundaries. Riverine runoff is based on modeled river discharges from the Norwegian Water Resources and Energy Directorate (Beldring et al., 2003).

     The model is initialized from the TOPAZ4 reanalysis on 1 January 2017 and run with 4D-Var assimilation of satellite SST and in situ temperature and salinity observations as described in Röhrs et al. (2018). This reanalysis is used to initialize a set of

70 different experiments (see Sect. 4.1), all of which assimilate only satellite SST observations and are run for the period 21 April 2018–22 June 2018.

The assimilation algorithm used for the experiments is the dual formulation of the ROMS 4D-Var system (RBL4DVAR; Moore et al., 2011; Gürol et al., 2014). Generally, in 4D-Var data assimilation, the analysis is found by minimizing a cost function in the form:

$$J(\boldsymbol{x}) = \frac{1}{2}(\boldsymbol{x} - \boldsymbol{x^b})^T \mathbf{B}^{-1}(\boldsymbol{x} - \boldsymbol{x^b}) + \frac{1}{2}(\boldsymbol{y} - \mathcal{H}(\boldsymbol{x}))^T \mathbf{R}^{-1}(\boldsymbol{y} - \mathcal{H}(\boldsymbol{x})), \tag{1}$$

where the control vector, $\boldsymbol{x}$, holds the control variables, which include the prognostic variables (temperature, salinity, horizontal velocity, and sea surface height) at the model grid points. The background control vector is denoted $\boldsymbol{x^b}$, while the vector $\boldsymbol{y}$ is the observations. In our setup, we gather the observations using a temporal spacing of 15 minutes. The observation operator, $\mathcal{H}$, returns the model equivalents of the observations by interpolating the model values to the observation locations. This interpolation is dynamic in nature since $\mathcal{H}$ includes the nonlinear model. In case the observed quantity is not part of the control vector, $\mathcal{H}$ may also transform the model values to correspond to the observed quantity. $\mathbf{B}$ is the background error covariance matrix, while $\mathbf{R}$ is the observation error covariance matrix. $\mathbf{R}$ is required to be diagonal in most operational data assimilation systems, including ROMS, as the 4D-Var minimization algorithm involves the inverse of $\mathbf{R}$ (e.g., Gürol et al., 2014). With a diagonal $\mathbf{R}$, we assume the observation errors to be uncorrelated in both time and space.

The observation errors used to construct $\mathbf{R}$ may represent the measurement error, which is the error associated with the accuracy of the measuring instrument, and representation errors (Janjić et al., 2018). The latter is connected to errors arising from the pre-processing and quality-control of the observations, the observation operator, and the mismatch between the resolutions of the observations and the model grid. In this study, the standard deviation of the error attributed to an observation (σ_o) is estimated as a function of the standard deviation of the background error at the observation location (σ_b), a factor based on the reported quality level of the satellite products (Q), and a parameter α:

$$\sigma_o^2 = \alpha \cdot Q \cdot \sigma_b^2. \tag{2}$$

The reported quality level reflects the uncertainty of the observation and is assigned to each SST measurement by the data creator (Donlon et al., 2007). Only quality level 4 (acceptable quality) and 5 (best quality) are used in this study. To ensure that more weight is given to the observations with best quality during assimilation, observations with quality levels 4 and 5 are assigned a Q of 1.1 and 0.9, respectively. The parameter α varies for each satellite product (Table 1) and is chosen by validating a set of experiments with different choices of α against independent data sets. Notice that for the PMW SSTs we use two different values for α: $\alpha = 0.3$ when the supermod operator (see Sect. 3) is activated, and $\alpha = 2$ when the supermod operator is not activated.

2.2 Observations

Satellite SST observations from IR and PMW radiometers are used in this study, and a summary of the products is found in Table 1. All observations are level-2 preprocessed (L2P) products downloaded from the Physical Oceanography Distributed Active Archive Center (PO.DAAC), the Satellite Application Facility on Ocean and Sea Ice (OSI SAF) FTP server, and the European Organisation for the Exploitation of Meteorological Satellites (EUMETSAT) data center online ordering client.

Table 1. IR and PMW satellite observations used in this study and their approximate spatial resolution at nadir. The factor α is used to estimate the observation errors (see Sect. 2.1).

Satellite	Sensor	Data creator	Method	Res. (km)	α
Metop-B	AVHRR	OSI SAF	IR	1.1	2
N20	VIIRS	NOAA	IR	0.75	2
GCOM-W1	AMSR-2	RSS	PMW	35×62	0.3 (2)
NPP	VIIRS	NOAA	IR	0.75	–
Sentinel-3A	SLSTR	EUMETSAT	IR	1	–

The IR SSTs have a spatial resolution ranging from 0.75–1.1 km at nadir and are thus capable of resolving SST structures of similar scales as the structures captured by the model. When several of these observations fall within the same model grid cell during the same time interval, the observations are averaged to create superobservations.

PMW radiometers can, contrary to IR radiometers, retrieve SSTs during cloudy conditions. Challenges related to PMW SST retrievals that require affected pixels to be discarded include rain, radio-frequency inference, sun glitter and emission from sea ice surfaces and land (Minnett et al., 2019). The latter contamination affects PMW retrievals from regions within $\sim$ 100 km from land. The spatial resolution of PMW SSTs depends on the frequency used to derive the SSTs and the antenna size and is significantly coarser than those of the IR SSTs. For AMSR-2 GCOM-W1, the primary band for PMW SST retrieval at 6.9 GHz corresponds to an elliptic footprint, elongated in the along-track direction of the satellite, with sizes of approximately 35 $\times$ 62 km (Imaoka et al., 2010).

All satellite SST observations are corrected by applying the single-sensor error statistics (SSES) bias, as recommended in Donlon et al. (2007). We use quality level 4 and 5 for the assimilated IR SST products. For the PMW SSTs, we use only quality level 5 observations and discard the quality level 4 observations due to unwanted artifacts in the SST field.

The SLSTR instrument onboard Sentinel-3A uses a dual view technique where the swath is scanned twice through two different atmospheric path lengths. This capability allows for more accurate SST measurements (Luo et al., 2020). Unlike the other SST products, which provide the sub-skin temperature, SLSTR Sentinel-3A provides the skin temperature. An offset of 0.17 °C is added to these skin temperatures so that all of the SSTs used throughout this study represent the sub-skin temperature (Donlon et al., 2002; Høyer et al., 2014). Due to the higher accuracy of the SLSTR sensor onboard Sentinel-3A, we use quality level 5 SSTs measured by this sensor to correct the other satellite products for biases (see Sect. 2.3) and for validation purposes. Other SSTs used for validation are bias-corrected SSTs from VIIRS NPP and SSTs measured by drifting buoys from the CORA data set (Cabanes et al., 2013). The spatial coverage of the drifting buoys is shown in Fig. 2.

Figure 3 shows time series of the number of observations inside the model domain during the chosen assimilation period in 2018. For the satellite observations, we count only observations meeting the set minimum quality level. Cloudiness causes the number of IR SST observations to vary. The largest number of observations is in the beginning of May, and there is a drop in
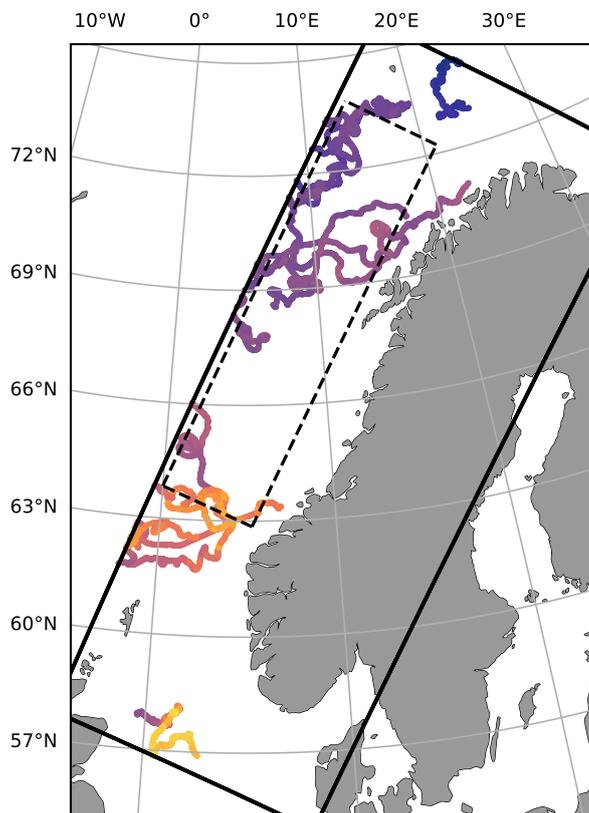
Figure 2. Colored lines show the spatial coverage of CORA drifting buoys during the period 21 April 2018–22 June 2018. There are in total ∼ 13 000 observations of this kind. Solid black box shows the extent of the model domain, while the dashed black box shows the domain selected for SST variance spectrum calculations (see Sect. 4.3).

the observational coverage while approaching June. The number of PMW SST observations is stable during the whole period, which we expect since PMW SSTs can be measured in cloudy conditions. Moreover, the number of available PMW SSTs is

130   on average smaller than the number of available IR SSTs since the PMW SSTs are provided on a coarser grid.

2.3 SST bias correction algorithm

High northern latitudes are recognized as challenging regions for satellite SST retrieval (Donlon et al., 2010; Wang et al., 2016; Jia and Minnett, 2020). In situ data are used to derive the satellite SST retrieval algorithms and to correct and thus improve the quality of the retrieved SST. However, the number of available in situ SST measurements at high northern latitudes is low

135   compared to equatorial and mid-latitude regions, and this data scarcity can lower the quality of high-latitude IR and PMW SST retrievals (O'Carroll et al., 2019).
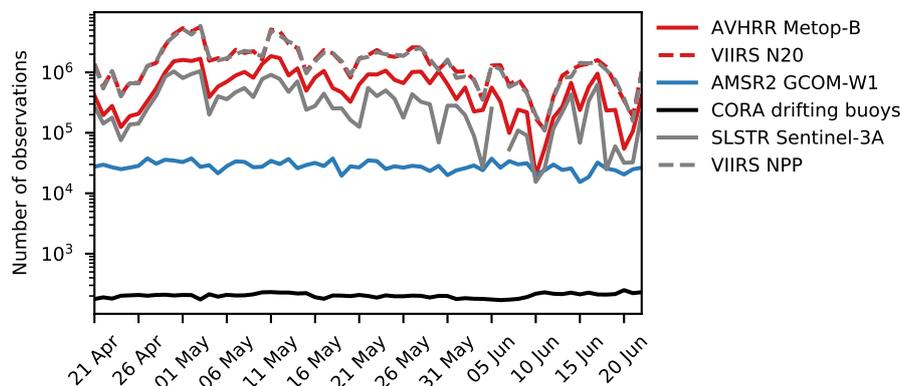
Figure 3. Time series of the number of observations available inside the model domain for each sensor and satellite pair and for the CORA drifting buoys.

The SST retrieval in the IR is subject to additional challenges. First, the process of cloud screening, where cloudy and clear-sky conditions are separated, is critical (O'Carroll et al., 2019). Any undetected clouds will result in erroneous SST retrievals. That the high northern latitudes are exposed to frequent cloud coverage challenges the identification process. Additionally,

140   the brightness temperatures derived from the measured IR radiance are modified by gases, such as water vapor, and aerosols in the atmosphere. Atmospheric correction algorithms are thus required to retrieve accurate SSTs. At high latitudes, these corrections tend to be problematic, hereby degrading the accuracy of the measured SSTs (Kumar et al., 2003; Merchant et al., 2006; Vincent, 2018; Jia and Minnett, 2020).

For the PMW part of the spectrum, challenges that must be corrected for (in addition to those mentioned in Sect. 2.2, which
145   cause the measurements to be discarded) include sea surface roughness generated from strong winds and atmospheric effects such as those associated with modification of the PMW radiation by water vapor and liquid water (Wentz et al., 2000; Minnett, 2014).

SST products from various satellites and sensors are subject to regional and temporal biases due to the difficulties concerning the SST retrieval process and the differences in applied retrieval algorithms (Chan and Gao, 2005; Høyer et al., 2012; Wang
150   et al., 2016). To this end, Høyer et al. (2014) developed and employed a bias correction scheme which they used to correct SST products from different providers. Their goal was to merge these products, and the correction was performed to avoid any biases from affecting the final product.

We implement a similar bias correction scheme, with some modifications, to ensure consistency between the different satellite SST products being assimilated into our model. The bias correction is an individual step during the preparation of ob-
155   servations for assimilation and is not part of the data assimilation process itself. Biases are calculated independently for all satellite products using SLSTR Sentinel-3A SST as reference. Figure 4 illustrates such a bias field for AVHRR Metop-B, and the method is described in what follows.
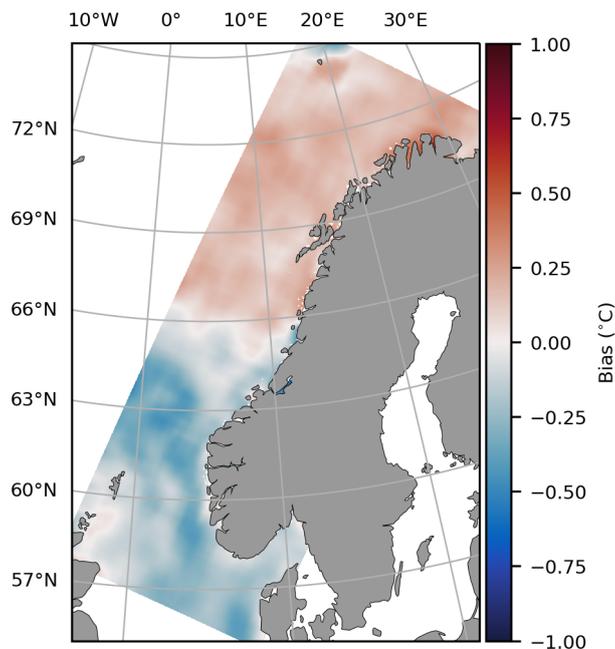
Figure 4. Mean bias for AVHRR Metop-B on 22 May 2018. The bias is calculated using 11 daily difference fields from 17 May 2018 to 27 May 2018.

Daily SST fields on a grid with a resolution of ∼ 25 km are produced for each satellite product, including the reference product, by first resampling the available L2P SST products to this coarser grid and then performing a simple averaging of the observations falling into each grid cell. To minimize the possibility of using SST observations affected by greater diurnal warming events (Eastwood et al., 2011; Karagali et al., 2012), we exclude observations located in regions where the wind speed is less than 3 m s^{-1} during local summer daytime (defined here as May–August at 10–14 UTC). This wind speed threshold is less strict than that recommended in Donlon et al. (2002) but was chosen to ensure sufficient spatial coverage in the daily fields.

Daily difference fields are produced by subtracting the reference daily SST field from the daily SST fields of the other satellite products. We remove all of the values where the difference exceeds ± 2 °C. This data removal is performed to exclude unrealistic values which we detected along the coast and nearby regions affected by cloud contamination.

By aggregating 11 daily difference fields, we produce a mean bias that is valid on the central day. The aggregation is performed as a simple temporal averaging as in Høyer et al. (2014). The bias correction scheme will thus correct for biases persistent for approximately 11 days. Correcting for biases occurring for shorter temporal scales would require a shorter temporal averaging interval, and additional reference SST products would have to be included to ensure sufficient spatial coverage. The mean biases are finally resampled to the model grid and, to avoid unwanted noise, spatially smoothed by applying a uniform filter. This filter has the size of 40 grid points (∼ 96 km) in both horizontal directions.

3 Supermod operator

175 As noted, observations with higher spatial resolution than the model are combined into superobservations. This procedure reduces the representation errors, as information on smaller spatial scales than what the model is able to represent is smoothed. For the case of PMW SST, however, each observation represents an SST average over the area covered by its footprint. For AMSR-2 GCOM-W1, this footprint is roughly 375 times larger than the area of a grid cell in our model domain. Thus, we expect the model to contain potentially valuable information on finer spatial scales than what is present in the observations.

180 If observations of this type were assimilated with a traditional observation operator that does not account for the observation footprints, we would expect large, spatially correlated representation errors (Liu and Rabier, 2002). Such errors are particularly problematic in operational data assimilation systems designed to handle uncorrelated observation errors.

An observation operator that ensures that each PMW SST observation is compared with a model mean over an equivalent area as the SST footprint is implemented in ROMS to avoid corrections of finer scales. The implementation of the operator

185 follows a similar methodology as described in Mile et al. (2021). We will refer to this operator as the supermod operator hereafter.

Our implementation of the supermod operator builds on the assumption that the observation footprints are squares with sides of length $(1+2L)dx$, where $(1+2L)$ is the number of grid cells and dx is the horizontal resolution of the model. L can be set separately for each individual observation, which makes the operator easy to apply to new observation sources and different

190 model configurations. As the center of the observation footprint may be located between model grid points, the supermod value is calculated as a weighted mean of the values in grid cells that fall completely or partially within the footprint area. This is done to conserve the effective resolution of the supermod values and to ensure that the model footprint is centered at the observation location. Another factor that could affect the effective resolution of the supermod values is the existence of land points within the footprint or if the footprint extends beyond the boundaries of the model domain. The operator is designed to

195 reject observations with these footprint features. Figure 5 illustrates how the operator works.

Idealized tests showed a sudden increase in the standard deviations of the innovations (observations minus background) when the footprints were increased and became overlapping. Thus, a thinning procedure is performed on the PMW observations prior to assimilating the observations. As the supermod operator can only represent square footprints, we have chosen L conservatively to make sure that the square used to represent the footprint will not be smaller than the largest size of the true,

200 elliptic footprint of the satellite retrievals. With the grid resolution of our model being 2.4 km, $L = 13$ gives us footprints with sides of 64.8 km. The PMW observations are thus thinned during a pre-processing step to ensure a distance of at least 64.8 km between the observation points.

3.1 Idealized experiment

An idealized scenario with no surface forcing, no land, and a flat bathymetry is applied in order to test the behavior of the

205 supermod operator in ROMS. A coarse grid with a horizontal resolution of $\sim$ 30 km is chosen to reduce the computational
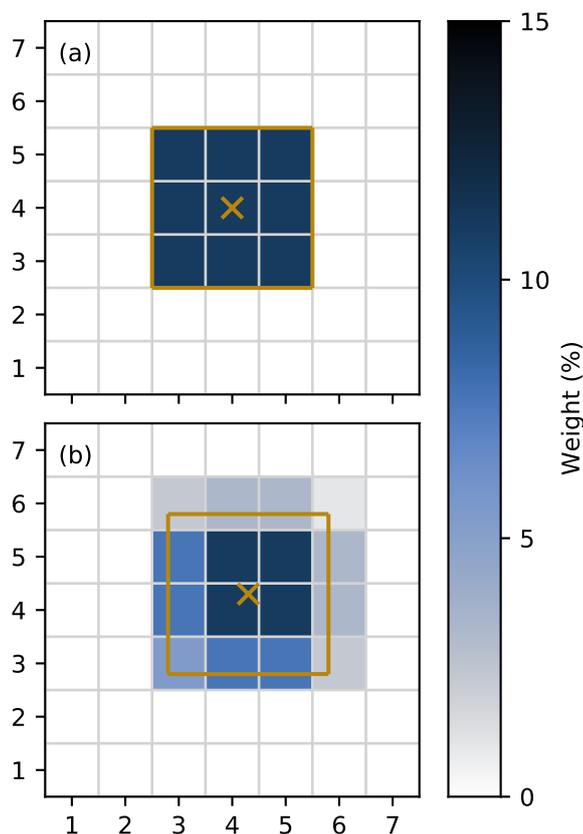
Figure 5. Schematic figure showing the supermod operator with $L = 1$ for (a) an observation that falls exactly in the center of a model grid cell; (b) an observation that is shifted towards the upper right corner of a grid cell. The orange crosses indicate the observation locations, the mesh illustrates grid cells, and the orange squares indicate the footprint area of the observations. The colormap indicates the weight (%) by which the grid cells contribute to the supermod value.

costs. The ocean is set to be initially at rest with a uniform temperature and salinity of 12 °C and 34, respectively. The standard deviations of the background errors are also uniform for every prognostic variable, and for temperature, it is set to 0.02 °C.

A single PMW SST observation, with a temperature of 12.5 °C and a standard deviation of the observation error set similar to the standard deviation of the background, is assimilated into the idealized setup for varying footprint sizes. Figure 6a–d show the resulting SST increments. Increasing the footprint size causes the increment to spread laterally such that the observation affects a greater area. The increment amplitude decreases simultaneously. Furthermore, for each footprint size in Fig. 6a–d, we calculate the average increment using all values greater than zero. That the average increment does not change significantly while increasing the footprint illustrates that the inclusion of the supermod operator spreads the information from the PMW SST observation as expected.
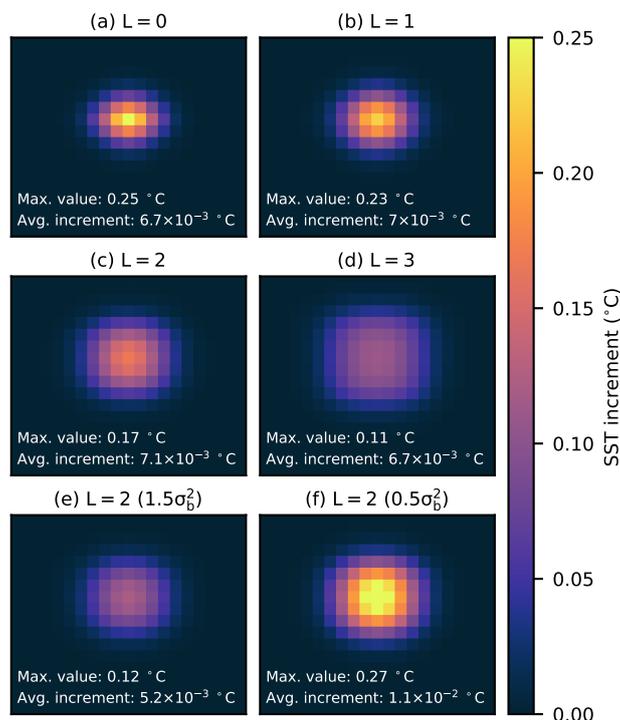
Figure 6. SST increment for (a–d) varying sizes of L and with the observation error (σ_o^2) set equal to the background error (σ_b^2); (e) $L = 2$ and $\sigma_o^2 = 1.5\sigma_b^2$; (f) $L = 2$ and $\sigma_o^2 = 0.5\sigma_b^2$.

Figure 6e and f show the effects of increasing and decreasing the observation error by a factor of 1.5 and 0.5, respectively, when the footprint parameter is set to $L = 2$. Increasing (decreasing) the error decreases (increases) the increment amplitude, which is what we would expect. Further tests revealed that the amplitude reduction with increasing L is not as pronounced when the observation error is set much smaller than the background error. In the extreme cases of a very small observation error, the increment might increase with increasing L.

4 Results

4.1 Experimental design

Different experiments are set up to (1) test the effect of correcting the satellite SSTs for biases before assimilation and (2) determine the effect of assimilating PMW SST observations with and without the application of the supermod operator. Table 2 summarizes the experiments, all of which cover the period 21 April 2018–22 June 2018.

To assess the bias correction scheme, IR SSTs are assimilated with (IR2) and without (IR1) applying a correction of biases. Similarly, to assess the supermod operator, we assimilate PMW SSTs by first treating the SSTs as regular point observa-

Table 2. Summary of experiments showing the sources (sensor and satellite) of the assimilated satellite SSTs, whether the observations are corrected for biases through the bias correction scheme, whether the supermod operator is activated, and the approximate number of observations assimilated (Nobs).

Experiment	Assimilated SST	Bias correction	Supermod	Nobs
IR1	AVHRR Metop-B VIIRS N20	No	–	2.4×10^7
IR2	AVHRR Metop-B VIIRS N20	Yes	–	2.4×10^7
PMW1	AMSR-2 GCOM-W1	Yes	No	1.7×10^6
PMW2	AMSR-2 GCOM-W1	Yes	Yes	2.3×10^4
COMB1	AVHRR Metop-B VIIRS N20 AMSR-2 GCOM-W1	Yes	No	2.5×10^7
COMB2	AVHRR Metop-B VIIRS N20 AMSR-2 GCOM-W1	Yes	Yes	2.4×10^7

tions (PMW1) and then by applying the supermod operator (PMW2). Notice that PMW2 includes the process of thinning the observations. As a consequence, PMW2 assimilates only $\sim 2\%$ of the observations assimilated in PMW1.

The argument for including PMW SSTs in the assimilated data set is to supplement the IR SSTs during periods of high
230 cloud coverage. Hence, we run two additional experiments to determine the effects of combining IR and PMW SSTs. In these experiments, we correct all of the observations for biases. Experiment COMB1 assimilates IR and PMW SSTs without employing the supermod operator, i.e., the experiment is a combination of IR2 and PMW1. The final experiment, COMB2, is a combination of IR2 and PMW2, thus assimilating IR and PMW SSTs with the supermod operator activated.

The assimilation window is set to three days in all experiments. The assimilated observations update the background pro-
235 duced for such a three-day cycle to produce the analysis. The ocean state at the end of the analysis is then used as the initial conditions for the next assimilation cycle, where a background is produced and the process repeats. Thus, the background can be considered a forecast, and we evaluate the experiments using the backgrounds in the following. If not stated otherwise, the evaluation period excludes the two first assimilation cycles and covers 27 April 2018–22 June 2018.

Table 3. SST RMSE (°C) and bias (°C). Validation metrics are calculated using SLSTR Sentinel-3A and bias-corrected VIIRS NPP SST as reference (left columns) and SSTs from drifting buoys as reference (right columns). Observations in coastal regions, where land emissions contaminate PMW SSTs, are excluded from the reference data sets.

	Satellites		Drifting buoys	
Experiment	RMSE	Bias	RMSE	Bias
IR1	0.534	−0.224	0.406	−0.173
IR2	0.470	−0.154	0.377	−0.143
PMW1	0.598	−0.177	0.402	−0.088
PMW2	0.612	−0.237	0.412	−0.121
COMB1	0.465	−0.143	0.368	−0.115
COMB2	0.468	−0.152	0.371	−0.142

4.2 Error statistics

240 Table 3 shows validation statistics in the SST for the background. In comparing IR1 and IR2, we find that correcting the observations for biases reduces the RMSE and the bias of the modeled SST. We expect improved statistics when validating against satellite SSTs since the validating data set contains SLSTR Sentinel-3A SSTs, which were the SSTs used to correct the observations assimilated in IR2. However, the in situ SSTs measured by drifting buoys are independent of the assimilated observations. The improvements in the error statistics calculated using this independent data set reveal the benefits of applying

245 the bias correction scheme.

The RMSE is higher in PMW1 than in IR2 both when validating against satellite and in situ SSTs. However, the bias of PMW1 is smaller than the bias of IR2 when validating against in situ SSTs, indicating that PMW SSTs are valuable to assimilate to reduce the model's systematic error. When validating against IR SSTs, PMW1 has a larger bias than IR2. This larger bias does not reflect the ability of the PMW SST data set to adjust the model but was found to be a direct consequence

250 of having no PMW observations in the coastal zones, causing the coastal current to be too cold during its heating phase as summer approaches.

Applying the supermod operator generally increases the errors, as can be seen by comparing PMW1 and PMW2. An explanation is that the increments in PMW2 are relatively weak compared to the increments in PMW1, which could be caused by both the observation thinning as well as how the supermod operator is designed to work (increasing the footprint results in a

255 decrease in the increment amplitude). Weaker increments cause smaller adjustments of the background and, depending on the capability of the PMW SSTs to represent the true state, greater errors during validation. The mean increment during the first assimilation window in PMW1 and PMW2, where both experiments have similar initial conditions, demonstrate this increment difference: the mean increment in PMW1 is ~ 0.48 °C (increment standard deviation: ~ 0.41 °C), whereas PMW2 has a mean
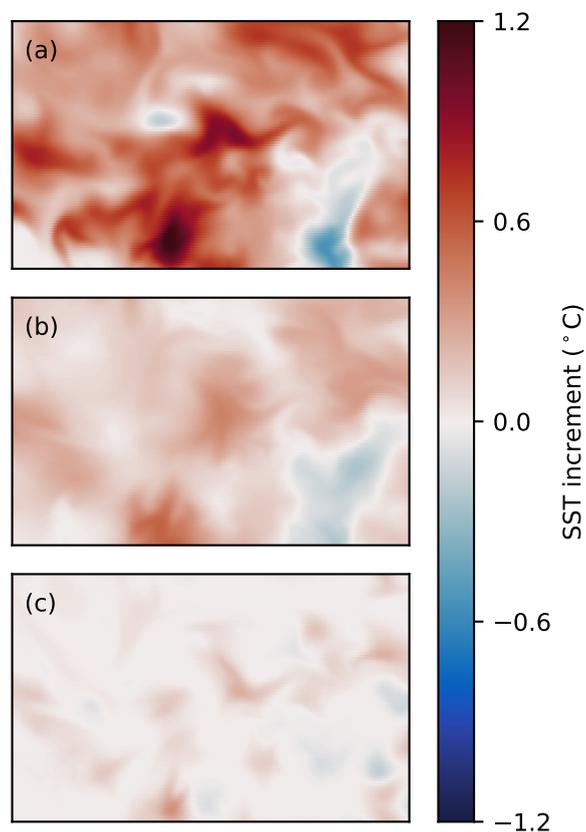
Figure 7. SST increments during the first time step in the first assimilation window shown for a selected region in the model domain. Increments belong to experiments (a) PMW1 and (b) PMW2. (c) shows the resulting increments if PMW1 assimilates observations thinned in the same way as the observations used in PMW2.

increment of ~ 0.21 °C (increment standard deviation: ~ 0.15 °C). The difference between the SST increment amplitudes in

260 PMW1 and PMW2 is, in addition, visually illustrated in Fig. 7a and b, which show the increments inside a selected region in the model domain. Even though the observations in PMW2 are thinned, the supermod operator is able to spread the impact of the observations over the footprint area to create an increment pattern which is similar to the pattern created in PMW1. However, the adjustments of the modeled SST are smaller in PMW2. That PMW2 is able to produce a similar increment pattern as PMW1, only with reduced increment amplitudes, indicates that the information provided by the additional SSTs in PMW1 is

265 redundant. This redundancy can be a symptom of significant correlations in the PMW SSTs observation error, as demonstrated by Liu and Rabier (2002). Assimilating a thinned version of the PMW SSTs without applying the supermod operator is, however, not sufficient to spread the increments over the observation footprint (Fig. 7c). The thinning itself does not handle the spatial resolution mismatch between the PMW SSTs and the model, and the supermod operator is required in order to spread the information from each observation over an area of similar size as the observation footprint.

270   Both COMB1 and COMB2 validate better than IR2, which implies that the PMW SST data set provides the model with information not seen by the IR SSTs and that the supermod operator is able to pass along this information. To ensure that these better validations are statistically significant, we performed a Monte Carlo approach where we randomly selected half of the calculated SST differences (model minus observations) for experiments IR2, COMB1, and COMB2, followed by a calculation of the SST RMSE and bias for each experiment. This selection and the subsequent calculations were repeated 1000 times.

275   Our tests showed that the better validation of COMB1 and COMB2 compared to IR2 is statistically significant at the 99 % level. Furthermore, we find that COMB1 validates better than COMB2. This can be explained by the differences between the magnitudes of the increments resulting from assimilating the PMW SST observations, as discussed when comparing PMW1 and PMW2. The better validation of COMB1 can also reflect that a smoothed version of a model field that resolves small-scale features generally validates better than the model field resolving these small-scale features. Small features captured by the

280   model tend to have incorrect positions compared to the reference observations used for validation (Dagestad and Röhrs, 2019; Jacobs et al., 2021).

We perform two additional validations to test if the improved error statistics of COMB1 and COMB2 can be explained by the additional information PMW SSTs bring to the model when IR SSTs are unavailable. First, we validate the background during the clear-sky period 6 May 2018–16 May 2018. Then, validation is performed during the cloudy period 7 June 2018–17

285   June 2018. We find that the cloudy period has an RMSE of 0.443 °C and 0.428 °C in IR2 and COMB2, respectively. The bias is −0.110 °C in IR2, while it is slightly reduced to −0.098 °C in COMB2. Conversely, the clear-sky period validation shows that both the RMSEs and biases are similar in IR2 and COMB2, differing only by 0.001 °C. Similar results are found when comparing IR2 and COMB1; that is, the RMSEs and biases differ the most during the cloudy period.

Figure 8 illustrates how PMW observations compensate for IR SST data deficiency. SST observations assimilated in IR2

290   during the assimilation cycle covering 8 June 2018–10 June 2018 are shown in Fig. 8a, while the SST increments from the beginning of this cycle at 8 June 2018 are shown in Fig. 8b. The presence of clouds limits the IR SST coverage, particularly in the southwestern part of the domain. A cluster of IR SST observations around the Shetland Islands causes a cooling of the model. However, the general lack of observations in this region leaves behind a larger area with no adjustments to the SST field. For COMB2, the assimilated observations and the increments are shown in Fig. 8c and d, respectively. We notice that

295   the regions without IR SST observations in Fig. 8a are now covered by PMW SSTs. This additional information to the model causes the SST field to adjust such that a larger area is cooled.

We suspect that the "blob" of warming between 58–59° N and 1–3° E in Fig. 8d arises from unwanted SST artifacts in the PMW SST data set. These artifacts are likely caused by radio-frequency interference from oil platforms (Alerskans et al., 2020). Careful consideration of the PMW SSTs revealed that it is not sufficient to discard all but the quality level 5 data to

300   avoid erroneous data. Thus, we will have to implement an additional quality-control which is based on the positions of oil platforms to use this PMW SST data set in the future.
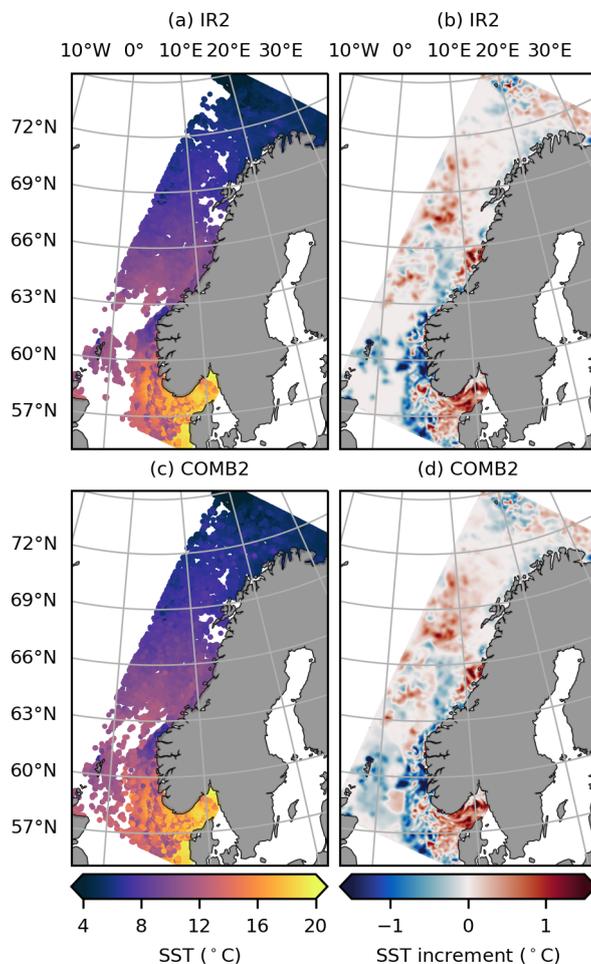
Figure 8. SST observations assimilated in (a) IR2 and (c) COMB2 during the assimilation cycle covering 8 June 2018–10 June 2018, and average SST increments at 8 June 2018 in (b) IR2 and (d) COMB2.

4.3 SST variance spectra

Spectral analysis is a technique that can be used to decompose the information contained in an observed or modeled field into different spatial scales. Specifically, spectra can be computed for modeled or observed SST fields to evaluate the spatial resolution of the SST structures contained within the field (e.g., Reynolds and Chelton, 2010; Brasnett and Colan, 2016; Castro et al., 2017; Pearson et al., 2019; Schubert et al., 2019; Janeković et al., 2022). The reason for this is that a spectrum holds information about the SST gradients at different spatial scales. A reduction in the spectral density at higher frequency scales (i.e., shorter wavelengths) thus reflects that the SST gradients at these scales have become weaker, i.e., that the field has become more smooth.

Usually, the SST data are decomposed into spectral space using the discrete Fourier transform (DFT), a transformation that requires the data to be periodic. Periodicity can be retained by spatially detrending the data or by windowing, i.e., multiplying the field by a function such that the interior of the domain retains its structures while the boundaries drop off and approach zero. A disadvantage of detrending and windowing is that these methods contaminate the largest scales in the spectral analysis (Denis et al., 2002). We use an alternative to the DFT to avoid these problems, namely the discrete cosine transform (DCT), where the input fields are made periodic in space by mirroring the fields prior to the transformation.

For each time step of the background, we apply the DCT to the two-dimensional SST field inside the dashed box shown in Fig. 2. This transformation into spectral space, as well as the subsequent calculation of the two-dimensional spectral variance array, follow the methodology described in Denis et al. (2002). The spectral variances are distributed between their corresponding wavelengths using the binning process presented in Ricard et al. (2013), so we end up with a one-dimensional SST variance spectrum. The SST variance spectra calculated for each time step are subsequently averaged in time to provide a mean SST variance spectrum.

Figure 9 shows the mean SST variance spectra calculated for each experiment (except IR1). For wavelengths smaller than ~ 120 km, we find that the spectrum from PMW1 has a significantly smaller variance than the spectrum calculated from IR2. Assimilating PMW SSTs without using the supermod operator has thus a smoothing effect on the modeled SST. This smoothing effect is also present in the spectrum calculated from COMB1, where IR SSTs are added to the assimilated data set: the spectrum from COMB1 follows that of PMW1 at most wavelengths and is more or less similar to PMW1's spectrum at wavelengths in the range ~ 35–120 km. This result is within expectations, as PMW SSTs represent a mean value over a large footprint of the actual SST field. With a traditional observation operator, this mean value is compared to individual model grid points, and any small-scale deviation from this mean value in the model is thus damped in the analysis.

The spectrum from PMW2 has more variance than that from IR2 at all scales smaller than ~ 200 km and follows the spectrum of a free model run (not shown). Furthermore, the variance spectrum from COMB2 is more or less identical to that of IR2 at all spatial scales. These findings suggest that using the supermod operator prevents the gradients present in the field from being smoothed: as PMW SSTs are now compared to mean model values, they do not penalize variations of the SST at spatial scales they do not resolve.

SST variance spectra were also calculated for each experiment using the last day of the analyses from each analysis cycle (not shown). The spectra were compared to the corresponding background spectra to examine if the assimilation changes the spatial scales of the background SST structures within each experiment. We find that the analyses in PMW1 experience a loss of SST structures with spatial scales of ~ 10–100 km and that the analyses in COMB1 have less SST structures at scales of ~ 50–70 km. The other experiments' analyses do not experience a significant loss due to the assimilation of the observations.

5 Discussion

Our results suggest that the PMW SSTs should be assimilated in conjunction with the IR SSTs in order to lower the errors in the modeled SST. This is verified by comparing error statistics of COMB1 and COMB2 to IR2. The comparison of error
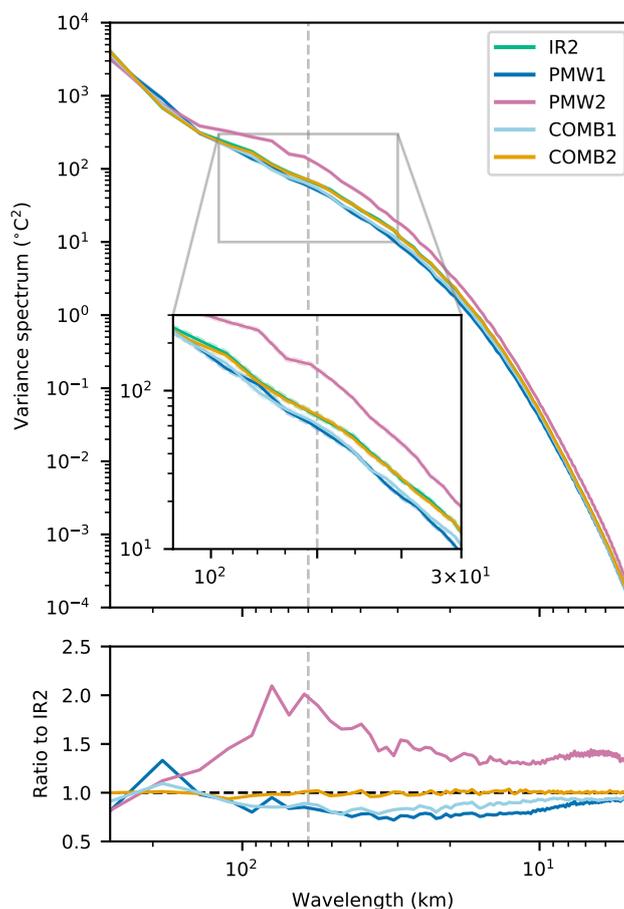
Figure 9. Upper panel shows SST variance spectra with wavelengths ranging from 278.4 km (length of the shortest edge of the domain used to calculate spectra) to 4.8 km (double the grid spacing). Shading is applied to indicate the 95 % confidence interval on the mean spectrum and is calculated using the jackknife method. Notice that the shading is hard to detect due to the smallness of the confidence interval. Inset zoom shows the spectra at wavelengths ranging from 120 km to 30 km. The lower panel shows the ratio of the experiments' spectra to the spectrum from IR2. A gray dashed line is drawn at 60 km, which is approximately the size of the major axis of the elliptic PMW SST footprint.

statistics during clear-sky and cloudy conditions imply that the error improvements in COMB1 and COMB2 originate from the additional information given to the model in cloudy regions where there is a shortage of IR SSTs. Figure 8, which shows the
345 SST increments in such cloudy regions, demonstrates the supermod operator's ability to pass along the relevant information seen by the PMW SSTs. The assimilated PMW SST observations cool the model SST in a region of sparse IR SST coverage. While the few available IR SSTs in that region confirm this cooling, they are not sufficient to correct the SST of the whole region when assimilated on their own.

While error statistics show that COMB1 validates better than COMB2, we find that COMB1 smooths SST structures. Hence, the smaller SST RMSE and bias of COMB1 do not reflect that this experiment is a better quality product. The smoothing of COMB1 is demonstrated by the calculated SST variance spectra. We find that both PMW1 and COMB1 return smoother SST fields than IR2 at spatial scales smaller than ~ 120 km. This upper limit is approximately twice the size of the major axis of the elliptic PMW SST footprint. Thus, the limit corresponds to the expected effective resolution of the SST structures resolved by the PMW SST observations. It is striking that the affected spatial scales in PMW1 and COMB1 correspond to scales smaller than or similar to this effective resolution. Furthermore, that the additional information from the IR SSTs in COMB1 does not prevent the smoothing reveals that the PMW SSTs greatly impact the final reanalysis product. However, assimilating the PMW SSTs through the supermod operator, which was performed in PMW2 and COMB2, does not result in a smoothing of the SST structures.

Finally, all of the experiments cover the local spring, which is a period when the modeled SST undergoes great changes. Such changes make it challenging to sustain high-skilled forecasts, and we chose the period due to these challenges. However, the chosen period is not heavily affected by clouds. The impact of assimilating PMW SSTs is possibly greater during winter when the oceanic regions along the Norwegian coastline experience high cloud coverage.

6 Conclusions

Correcting the satellite SSTs for biases through the implemented bias correction scheme improves the modeled SST. The bias correction scheme is easy to implement and apply since it is separate from the data assimilation process.

While assimilating IR SSTs reduces the modeled SST errors, an additional reduction is achieved if PMW SSTs are assimilated in conjunction with the IR SSTs. This error reduction is mainly caused by the information the PMW SSTs provide in cloudy regions. However, if we assimilate the PMW SSTs without considering their large footprint sizes, we end up smoothing the modeled SST structures of spatial scales smaller than twice the PMW SST footprint. By introducing the supermod operator, we have shown that the PMW SST observations can be assimilated into the ocean model without causing any spatial smoothing of the modeled SST. Our supermod operator is easy to implement and can be used to assimilate other observation variables having a coarser spatial resolution than the resolution of the model.

Code and data availability. Code for implementing the supermod operator is available at: https://github.com/siljeci/ROMS_supermod. Model output from each data assimilation experiment is available at: https://thredds.met.no/thredds/projects/supermodop.html.

Author contributions. SCI: Conceptualization, Data curation, Formal analysis, Investigation, Methodology, Software, Validation, Visualization, Writing – original draft preparation, Writing - review & editing. AKS: Conceptualization, Data curation, Methodology, Project administration, Supervision, Validation, Writing - review & editing. OG: Formal analysis, Software, Validation, Writing - review & editing.

Competing interests. The contact author has declared that none of the authors has any competing interests.

Acknowledgements. This research was funded by the Centre of Integrated Remote Sensing and Forecasting for Arctic Operations (CIRFA)
380 under the Research Council of Norway (RCN), grant number 237906. Data from the European Organisation for the Exploitation of Me-
teorological Satellites (EUMETSAT) Satellite Application Facility on Ocean and Sea Ice (OSI SAF) are accessible through https://osi-
saf.eumetsat.int. Data were also provided by Group for High Resolution Sea Surface Temperature (GHRSST), the National Oceanic and
Atmospheric Administration (NOAA) and Remote Sensing Systems (RSS). These data can be downloaded from he Physical Oceanography
Distributed Active Archive Center (PO.DAAC). Data were also created and distributed by EUMETSAT.

References

Alerskans, E., Høyer, J. L., Gentemann, C. L., Pedersen, L. T., Nielsen-Englyst, P., and Donlon, C.: Construction of a climate data record of sea surface temperature from passive microwave measurements, Remote Sens. Environ., 236, 111 485, https://doi.org/10.1016/j.rse.2019.111485, 2020.

Beldring, S., Engeland, K., Roald, L., Sælthun, N., and Voksø, A.: Estimation of parameters in a distributed precipitation-runoff model for Norway, Hydrol. Earth Syst. Sci., 7, 304–316, https://doi.org/10.5194/hess-7-304-2003, 2003.

Brasnett, B. and Colan, D. S.: Assimilating Retrievals of Sea Surface Temperature from VIIRS and AMSR2, J. Atmos. Ocean Tech., 33, 361–375, https://doi.org/10.1175/JTECH-D-15-0093.1, 2016.

Buehner, M., Caya, A., Pogson, L., Carrieres, T., and Pestieau, P.: A New Environment Canada Regional Ice Analysis System, Atmos. Ocean, 51, 18–34, https://doi.org/10.1080/07055900.2012.747171, 2013.

Cabanes, C., Grouazel, A., von Schuckmann, K., Hamon, M., Turpin, V., Coatanoan, C., Paris, F., Guinehut, S., Boone, C., Ferry, N., de Boyer Montégut, C., Carval, T., Reverdin, G., Pouliquen, S., and Le Traon, P.-Y.: The CORA dataset: validation and diagnostics of in-situ ocean temperature and salinity measurements, Ocean Sci., 9, 1–18, https://doi.org/10.5194/os-9-1-2013, 2013.

Castro, S., Emery, W., Wick, G., and Tandy, W.: Submesoscale Sea Surface Temperature Variability from UAV and Satellite Measurements, Remote Sens., 9, 1089, https://doi.org/10.3390/rs9111089, 2017.

Chan, P.-K. and Gao, B.-C.: A Comparison of MODIS, NCEP, and TMI Sea Surface Temperature Datasets, IEEE Geosci. Remote S., 2, 270–274, https://doi.org/10.1109/LGRS.2005.846838, 2005.

Dagestad, K.-F. and Röhrs, J.: Prediction of ocean surface trajectories using satellite derived vs. modeled ocean currents, Remote Sens. Environ., 223, 130–142, https://doi.org/10.1016/j.rse.2019.01.001, 2019.

Denis, B., Côté, J., and Laprise, R.: Spectral Decomposition of Two-Dimensional Atmospheric Fields on Limited-Area Domains Using the Discrete Cosine Transform (DCT), Mon. Weather Rev., 130, 1812–1829, https://doi.org/10.1175/1520-0493(2002)130<1812:SDOTDA>2.0.CO;2, 2002.

Donlon, C. J., Minnett, P. J., Gentemann, C., Nightingale, T. J., Barton, I. J., Ward, B., and Murray, M. J.: Toward Improved Validation of Satellite Sea Surface Skin Temperature Measurements for Climate Research, J. Climate, 15, 353–369, https://doi.org/10.1175/1520-0442(2002)015<0353:TIVOSS>2.0.CO;2, 2002.

Donlon, C. J., Robinson, I., Casey, K. S., Vazquez-Cuervo, J., Armstrong, E., Arino, O., Gentemann, C., May, D., LeBorgne, P., Piollé, J., Barton, I., Beggs, H., Poulter, D. J. S., Merchant, C. J., Bingham, A., Heinz, S., Harris, A., Wick, G., Emery, B., Minnett, P., Evans, R., Llewellyn-Jones, D., Mutlow, C., Reynolds, R. W., Kawamura, H., and Rayner, N.: The Global Ocean Data Assimilation Experiment High-resolution Sea Surface Temperature Pilot Project, B. Am. Meteorol. Soc., 88, 1197–1214, https://doi.org/10.1175/BAMS-88-8-1197, 2007.

Donlon, C. J., Casey, K., Gentemann, C., LeBorgne, P., Robinson, I., Reynolds, R. W., Merchant, C., Llewellyn-Jones, D., Minnett, P. J., Piolle, J. F., Cornillon, P., Rayner, N., Brandon, T., Vazquez, J., Armstrong, E., Beggs, H., Barton, I., Wick, G., Castro, S., Høyer, J., May, D., Arino, O., Poulter, D. J., Evans, R., Mutlow, C. T., Bingham, A. W., and Harris, A.: Successes and Challenges for the Modern Sea Surface Temperature Observing System, in: Proceedings of OceanObs'09: Sustained Ocean Observations and Information for Society, vol. 2, pp. 249–258, ESA Publication WPP-306, Venice, Italy, https://doi.org/10.5270/OceanObs09.cwp.24, 2010.

Donlon, C. J., Martin, M.and Stark, J., Roberts-Jones, J., Fiedler, E., and Wimmer, W.: The Operational Sea Surface Temperature and Sea Ice Analysis (OSTIA) system, Remote Sens. Environ., 116, 140–158, https://doi.org/10.1016/j.rse.2010.10.017, 2012.

Eastwood, S., Le Borgne, P., Péré, S., and Poulter, D.: Diurnal variability in sea surface temperature in the Arctic, Remote Sens. Environ., 115, 2594–2602, https://doi.org/10.1016/j.rse.2011.05.015, 2011.

ECMWF: ECMWF IFS CY41r2 High-Resolution Operational Forecasts, Research Data Archive at the National Center for Atmospheric Research, Computational and Information Systems Laboratory [data set], https://doi.org/10.5065/D68050ZV, accessed 11 March 2020, 2016.

Egbert, G. D. and Erofeeva, S. Y.: Efficient Inverse Modeling of Barotropic Ocean Tides, J. Atmos. Ocean. Tech., 19, 183–204, https://doi.org/10.1175/1520-0426(2002)019<0183:EIMOBO>2.0.CO;2, 2002.

Fairall, C. W., Bradley, E. F., Hare, J. E., Grachev, A. A., and Edson, J. B.: Bulk parameterization of air–sea fluxes: Updates and verification for the COARE algorithm, J. Climate, 16, 571–591, https://doi.org/10.1175/1520-0442(2003)016<0571:BPOASF>2.0.CO;2, 2003.

Gürol, S., Weaver, A. T., Moore, A. M., Piacentini, A., Arango, H. G., and Gratton, S.: B-preconditioned minimization algorithms for variational data assimilation with the dual formulation, Q. J. Roy. Meteor. Soc., 140, 539–556, https://doi.org/10.1002/qj.2150, 2014.

Haidvogel, D. B., Arango, H., Budgell, W. P., Cornuelle, B. D., Curchitser, E., Di Lorenzo, E., Fennel, K., Geyer, W. R., Hermann, A. J., Lanerolle, L., Levin, J., McWilliams, J. C., Miller, A. J., Moore, A. M., Powell, T. M., Shchepetkin, A. F., Sherwood, C. R., Signell, R. P., Warner, J. C., and Wilkin, J.: Ocean forecasting in terrain-following coordinates: Formulation and skill assessment of the Regional Ocean Modeling System, J. Comput. Phys., 227, 3595–3624, https://doi.org/10.1016/j.jcp.2007.06.016, 2008.

Høyer, J. L., Karagali, I., Dybkjær, G., and Tonboe, R.: Multi sensor validation and error characteristics of Arctic satellite sea surface temperature observations, Remote Sens. Environ., 121, 335–346, https://doi.org/10.1016/j.rse.2012.01.013, 2012.

Høyer, J. L., Le Borgne, P., and Eastwood, S.: A bias correction method for Arctic satellite sea surface temperature observations, Remote Sens. Environ., 146, 201–213, https://doi.org/10.1016/j.rse.2013.04.020, 2014.

Imaoka, K., Kachi, M., Kasahara, M., Ito, N., Nakagawa, K., and Oki, T.: Instrument performance and calibration of AMSR-E and AMSR2, Int. Arch. Photogramm., 38, 13–18, 2010.

Jacobs, G. A., D'Addezio, J. M., Bartels, B., and Spence, P. L.: Constrained scales in ocean forecasting, Adv. Space Res., 68, 746–761, https://doi.org/10.1016/j.asr.2019.09.018, 2021.

Janeković, I., Rayson, M., Jones, N., Watson, P., and Pattiaratchi, C.: 4D-Var data assimilation using satellite sea surface temperature to improve the tidally-driven interior ocean dynamics estimates in the Indo-Australian Basin, Ocean Model., 171, 101 969, https://doi.org/10.1016/j.ocemod.2022.101969, 2022.

Janjić, T., Bormann, N., Bocquet, M., Carton, J. A., Cohn, S. E., Dance, S. L., Losa, S. N., Nichols, N. K., Potthast, R., Waller, J. A., and Weston, P.: On the representation error in data assimilation, Q. J. Roy. Meteor. Soc., 144, 1257–1278, https://doi.org/10.1002/qj.3130, 2018.

Jia, C. and Minnett, P. J.: High latitude sea surface temperatures derived from MODIS infrared measurements, Remote Sens. Environ., 251, 112 094, https://doi.org/10.1016/j.rse.2020.112094, 2020.

Karagali, I., Høyer, J., and Hasager, C.: SST diurnal variability in the North Sea and the Baltic Sea, Remote Sens. Environ., 121, 159–170, https://doi.org/10.1016/j.rse.2012.01.016, 2012.

Kumar, A., Minnett, P. J., Podestá, G., and Evans, R. H.: Error Characteristics of the Atmospheric Correction Algorithms Used in Retrieval of Sea Surface Temperatures from Infrared Satellite Measurements: Global and Regional Aspects, J. Atmos. Sci., 60, 575–585, https://doi.org/10.1175/1520-0469(2003)060<0575:ECOTAC>2.0.CO;2, 2003.

Liu, Z.-Q. and Rabier, F.: The interaction between model resolution, observation resolution and observation density in data assimilation: A one-dimensional study, Q. J. Roy. Meteor. Soc., 128, 1367–1386, https://doi.org/10.1256/003590002320373337, 2002.

460 Luo, B., Minnett, P. J., Szczodrak, M., Kilpatrick, K., and Izaguirre, M.: Validation of Sentinel-3A SLSTR derived Sea-Surface Skin Tem-
peratures with those of the shipborne M-AERI, Remote Sens. Environ., 244, 111 826, https://doi.org/10.1016/j.rse.2020.111826, 2020.

Martin, M. J., King, R. R., While, J., and Aguiar, A. B.: Assimilating satellite sea-surface salinity data from SMOS, Aquarius and SMAP
into a global ocean forecasting system, Q. J. Roy. Meteor. Soc., 145, 705–726, https://doi.org/10.1002/qj.3461, 2019.

Merchant, C. J., Embury, O., Le Borgne, P., and Bellec, B.: Saharan dust in nighttime thermal imagery: Detection and reduction of related
465 biases in retrieved sea surface temperature, Remote Sens. Environ., 104, 15–30, https://doi.org/10.1016/j.rse.2006.03.007, 2006.

Mile, M., Randriamampianina, R., Marseille, G., and Stoffelen, A.: Supermodding – A special footprint operator for mesoscale data assimi-
lation using scatterometer winds, Q. J. Roy. Meteor. Soc., 147, 1382–1402, https://doi.org/10.1002/qj.3979, 2021.

Minnett, P. J.: Sea Surface Temperature, in: Encyclopedia of Remote Sensing, edited by Njoku, E. G., pp. 754–759, Springer New York,
https://doi.org/10.1007/978-0-387-36699-9_166, 2014.

470 Minnett, P. J., Alvera-Azcárate, A., Chin, T. M., Corlett, G. K., Gentemann, C. L., Karagali, I., Li, X., Marsouin, A., Marullo, S., Maturi, E.,
Santoleri, R., Saux Picart, S., Steele, M., and Vazquez-Cuervo, J.: Half a century of satellite remote sensing of sea-surface temperature,
Remote Sens. of Environ., 233, 111 366, https://doi.org/10.1016/j.rse.2019.111366, 2019.

Moore, A. M., Arango, H. G., Broquet, G., Powell, B. S., Weaver, A. T., and Zavala-Garay, J.: The Regional Ocean Modeling System
(ROMS) 4-dimensional variational data assimilation systems. Part I - System overview and formulation, Prog. Oceanogr., 91, 34–49,
475 https://doi.org/10.1016/j.pocean.2011.05.004, 2011.

O'Carroll, A. G., Armstrong, E. M., Beggs, H. M., Bouali, M., Casey, K. S., Corlett, G. K., Dash, P., Donlon, C. J., Gentemann, C. L., Høyer,
J. L., Ignatov, A., Kabobah, K., Kachi, M., Kurihara, Y., Karagali, I., Maturi, E., Merchant, C. J., Marullo, S., Minnett, P. J., Pennybacker,
M., Ramakrishnan, B., Ramsankaran, R., Santoleri, R., Sunder, S., Saux Picart, S., Vázquez-Cuervo, J., and Wimmer, W.: Observational
Needs of Sea Surface Temperature, Front. Mar. Sci., 6, 420, https://doi.org/10.3389/fmars.2019.00420, 2019.

480 Pearson, K., Good, S., Merchant, C. J., Prigent, C., Embury, O., and Donlon, C.: Sea Surface Temperature in Global Analyses: Gains from
the Copernicus Imaging Microwave Radiometer, Remote Sens., 11, 2362, https://doi.org/10.3390/rs11202362, 2019.

Reynolds, R. W. and Chelton, D. B.: Comparisons of Daily Sea Surface Temperature Analyses for 2007–08, J. Climate, 23, 3545–3562,
https://doi.org/10.1175/2010JCLI3294.1, 2010.

Ricard, D., Lac, C., Riette, S., Legrand, R., and Mary, A.: Kinetic energy spectra characteristics of two convection-permitting limited-area
485 models AROME and Meso-NH: KE Spectra Characteristics of Two Convection-Permitting Models, Q. J. Roy. Meteor. Soc., 139, 1327–
1341, https://doi.org/10.1002/qj.2025, 2013.

Röhrs, J., Sperrevik, A. K., and Christensen, K. H.: NorShelf: An ocean reanalysis and data-assimilative forecast model for the Norwegian
Shelf Sea, Tech. Rep. ISSN 2387-4201 04/2018, Norwegian Meteorological Institute, Oslo, Norway, https://www.met.no/publikasjoner/
met-report, 2018.

490 Schubert, R., Schwarzkopf, F. U., Baschek, B., and Biastoch, A.: Submesoscale Impacts on Mesoscale Agulhas Dynamics, J. Adv. Model.
Earth Sy., 11, 2745–2767, https://doi.org/10.1029/2019MS001724, 2019.

Shchepetkin, A. F. and McWilliams, J. C.: Correction and commentary for "Ocean forecasting in terrain-following coordinates: Formulation
and skill assessment of the regional ocean modeling system" by Haidvogel et al., J. Comp. Phys. 227, pp. 3595–3624, J. Comput. Phys.,
228, 8985–9000, https://doi.org/10.1016/j.jcp.2009.09.002, 2009.

495 Umlauf, L. and Burchard, H.: Second-order turbulence closure models for geophysical boundary layers. A review of recent work, Cont. Shelf
Res., 25, 795–827, https://doi.org/10.1016/j.csr.2004.08.004, 2005.

Vincent, R. F.: The Effect of Arctic Dust on the Retrieval of Satellite Derived Sea and Ice Surface Temperatures, Sci. Rep., 8, 9727, https://doi.org/10.1038/s41598-018-28024-6, 2018.

Wang, H., Guan, L., and Chen, G.: Evaluation of Sea Surface Temperature From FY-3C VIRR Data in the Arctic, IEEE Geosci. Remote S.,
500   13, 292–296, https://doi.org/10.1109/LGRS.2015.2511184, 2016.

Warner, J. C., Sherwood, C. R., Arango, H. G., and Signell, R. P.: Performance of four turbulence closure models implemented using a generic length scale method, Ocean Model., 8, 81–113, https://doi.org/10.1016/j.ocemod.2003.12.003, 2005.

Wentz, F. J., Gentemann, C., Smith, D., and Chelton, D.: Satellite Measurements of Sea Surface Temperature Through Clouds, Science, 288, 847–850, https://doi.org/10.1126/science.288.5467.847, 2000.

505   Xie, J., Bertino, L., Counillon, F., Lisæter, K. A., and Sakov, P.: Quality assessment of the TOPAZ4 reanalysis in the Arctic over the period 1991–2013, Ocean Sci., 13, 123–144, https://doi.org/10.5194/os-13-123-2017, 2017.